

Optical and Far-UV Spectroscopy of Knot D in the Vela Supernova Remnant

Ravi Sankrit, William P. Blair

The Johns Hopkins University

Department of Physics and Astronomy, 3400 N. Charles St., Baltimore, MD 21218

ravi@pha.jhu.edu, wpb@pha.jhu.edu

and

John C. Raymond

Harvard-Smithsonian Center for Astrophysics, 60, Garden St., Cambridge, MA 02138

jraymond@cfa.harvard.edu

ABSTRACT

We present spectra of optical filaments associated with the X-ray knot D in the Vela supernova remnant. It has been suggested that Knot D is formed by a bullet of supernova ejecta, that it is a break-out of the shock front of the Vela SNR, and also that it is an outflow from the recently discovered remnant RXJ0852.0-4622. We find that Knot D is a bow shock propagating into an interstellar cloud with normal abundances and typical cloud densities ($n_{\text{H}} \sim 4 - 11 \text{ cm}^{-3}$). Optical longslit spectra show that the [S II] $\lambda\lambda 6716, 6731$ to $\text{H}\alpha$ line ratio is greater than unity, proving that the optical filaments are shock excited. The analysis of far-ultraviolet spectra obtained with the Hopkins Ultraviolet Telescope and with the Far Ultraviolet Spectroscopic Explorer (FUSE) LWRS aperture show that slower shocks ($\sim 100 \text{ km s}^{-1}$) produce most of the low ionization lines such as O III] $\lambda 1662$, while faster shocks ($\sim 180 \text{ km s}^{-1}$) produce the O VI $\lambda\lambda 1032, 1038$ and other high ionization lines. C III and O VI lines are also detected in the FUSE MDRS aperture, which was located on an X-ray bright region away from the optical filaments. The lines have two velocity components consistent with $\sim 150 \text{ km s}^{-1}$ shocks on the near and far sides of the knot. The driving pressure in the X-ray knot, $P/k_{\text{B}} \sim 1.8 \times 10^7 \text{ cm}^{-3} \text{ K}$, is derived from the shock properties.

This is over an order of magnitude larger than the characteristic X-ray pressure in the Vela SNR. The velocity distribution of the emission and the overpressure support the idea that Knot D is a bow shock around a bullet or cloud that originated near the center of the Vela remnant.

Subject headings: ISM: individual (Vela) — ISM: supernova remnants — shock waves

1. Introduction

In an X-ray image obtained with ROSAT, the Vela Supernova Remnant (SNR) is roughly circular with a diameter $\sim 8^\circ$ (Aschenbach, Egger & Trümper 1995). At a distance of 250 pc (Cha, Sembach & Danks 1999) this corresponds to about 35 pc. Six bow shaped “knots” of emission lie beyond the nominal circumference of the remnant. The shape and location of these knots led Aschenbach et al. to suggest that they were due to ejecta “bullets” that had overtaken the blast wave. Of the six features, the closest to the remnant and also the brightest in X-ray is “Knot D”. The optical nebula RCW 37 (Rodgers, Campbell & Whiteoak 1960), lies along the outer edge of Knot D. This association with bright optical filaments also distinguishes Knot D from the other five knots.

Although it is grouped with the ejecta bullets, there are two other explanations for the origin of Knot D. One scenario, suggested by Plucinsky et al. (2002) is that Knot D is a shock that has broken out from the Vela SNR due to inhomogeneities in the ambient medium. They analyzed *Chandra*-ACIS spectra of Knot D and found that the oxygen abundance was solar and that the neon abundance was modestly enhanced, and they found no evidence for abundance differences at different locations in the knot. These results as well as the morphology of the X-ray emission led Plucinsky et al. (2002) to favor a shock break-out origin for Knot D. The other suggestion (Redman et al. 2000, 2002) is that Knot D is associated with RXJ0852.0-4622, a remnant that in projection is within the boundaries of the Vela SNR. They analyzed optical echelle data of RCW 37 and found a velocity split near the bright optical edge in both [S II] and [O III] emission, and an almost complete velocity ellipse across the nebula in the latter. They inferred that the geometry of the optical nebula is either an incomplete funnel or a wavy sheet. Based on the kinematic structure of emission as well as the optical and X-ray morphologies of the nebula they suggested that an outflow from RXJ0852.0-4622 impacted the pre-existing wall of the Vela SNR to produce Knot D. As they point out, for their model to work both remnants have to be at about the same distance (Redman et al. 2002).

Regardless of its origin, it is known that Knot D is a source of shock excited emission. Blair, Vancura & Long (1995) presented far-ultraviolet observations of the region obtained with the *Voyager 2* Ultraviolet Spectrometer. Strong emission from C III $\lambda 977$ and O VI $\lambda\lambda 1032, 1038$ was detected in the spectrum. The authors noted the sheet-like morphology of the filaments and the spatial coincidence of the X-ray and optical emission and argued that these were characteristics of a shock-cloud interaction (such as had been seen in the Cygnus Loop SNR) and that this interaction produced the ultraviolet lines as well as the optical emission. They suggested that the large *Voyager* FOV included shocks with a range of velocities, and that $\sim 120 \text{ km s}^{-1}$ shocks were responsible for the C III emission and $160\text{--}300 \text{ km s}^{-1}$ shocks produced the O VI emission.

In this paper we take a detailed look at the shock-cloud interaction and determine the shock wave parameters. Our results throw some light on the nature of Knot D, but do not unambiguously determine its origin. We use ultraviolet spectra obtained with the *Hopkins Ultraviolet Telescope* (HUT) and with the *Far Ultraviolet Spectroscopic Explorer* (FUSE). These data have much higher spectral resolution than the *Voyager* spectrum and the aperture FOVs are over a thousand times smaller. We also present optical longslit spectra of the filaments. We confirm that the optical emission is shock excited. By comparing the measured far-ultraviolet emission line strengths with shock model predictions, we find the properties of the shocks around Knot D. The kinematic distribution of the emission around the bow shock is clearly revealed in the high resolution FUSE data. The observations are described in §2, and the results presented in §3. Then, in §4 we analyze the results and present our interpretation. The last section, §5 summarizes the central results of this work and presents some of the issues yet to be answered.

2. Observations

Images of the region of interest are shown in Figure 1. The top panel is a three color image of the southern half of Knot D. Narrowband $H\alpha$ and [O III] $\lambda 5007$ images (first presented by Blair, Vancura & Long (1995)) are shown in red and green, respectively. The blue is the *Chandra* X-ray image, presented by Plucinsky et al. (2002) (and kindly provided to us by the lead author). Overlaid on the image are the locations of the FUSE LWRS and MDRS apertures. The bottom panel is a two color image of a region around the bright filament. Only the optical emission is shown ($H\alpha$ in red, [O III] in green) overlaid with the HUT and FUSE LWRS aperture positions.

The HUT observations were made during the Astro-2 space shuttle mission on 1995 March 15. (The basic HUT design is described by Davidsen et al. (1992), and the improve-

ments to the instrument for Astro-2 by Kruk et al. (1995).) The wavelength coverage of HUT was $820 - 1840\text{\AA}$ with a resolution of $\sim 3\text{\AA}$. The $56'' \times 10''$ aperture was centered at $\alpha_{2000} = 09^{\text{h}}00^{\text{m}}24^{\text{s}}.30$, $\delta_{2000} = -45^{\circ} 54' 31''.5$, and placed at a position angle of 18° which aligned the aperture with the optical filament. After approximately 1000 s of exposure time at this position, the aperture was offset to a location $\sim 30''$ East, perpendicular to the aperture's long dimension. We refer to these positions as P1 and P2, respectively (Figure 1b). The data were obtained in a time-tag mode which allowed the separation of orbital day and night photons. Since the daytime photons are contaminated by airglow emission, only the nighttime data are used here. The effective exposure times are 932 s for P1 and 1162 s for P2.

The HUT data were processed using an IRAF¹ package originally developed to process HUT data from the Astro-1 mission, and described by Kruk et al. (1999). The flux calibration applied to these data is based on in-orbit observations of white dwarf stars fitted with theoretical models. Other corrections, such as pulse persistence, dark count and Ly α scattering have been characterized and included here (Kruk et al. 1995, 1999).

The FUSE observation (Program ID B1080201) was obtained on 2001 April 2 as part of a Guest Investigator project to study the Vela-Puppis region. Eleven exposures with a total integration time of 14,133 s were obtained with the low resolution (LWRS) $30'' \times 30''$ aperture centered at $\alpha_{2000} = 09^{\text{h}}00^{\text{m}}24^{\text{s}}.30$, $\delta_{2000} = -45^{\circ} 54' 31''.5$. This position is the same as the center of the HUT P1 observation, and lies on the bright optical filament (Figure 1b). Data were obtained simultaneously through the medium resolution (MDRS) $20'' \times 4''$ aperture. The MDRS aperture was located $208''$ away, 24° West of North from the LWRS aperture on an X-ray bright region away from the bright optical emission (Figure 1a).

The wavelength range covered by FUSE is $905 - 1187\text{\AA}$. In this paper we present data from segments SiC2A ($\sim 905 - 1000\text{\AA}$), LiF1A ($\sim 1000 - 1100\text{\AA}$) and LiF2A ($\sim 1100 - 1187\text{\AA}$), the segments with largest effective area in their wavelength ranges (Moos et al. 2000). The data in other segments were used for comparison to distinguish between real features and possible detector artifacts. The raw data from all the exposures were combined and the pipeline CalFUSE version 1.8.7 was used to produce calibrated spectra. A shift was applied to the LiF1A and SiC2A flux vectors to line up the geocoronal emission (Ly β and Ly γ respectively for the two channels) at the appropriate wavelength in the heliocentric frame of reference. This was done for both LWRS and MDRS spectra. The source is an extended

¹IRAF is distributed by the National Optical Astronomy Observatories, which are operated by the Association of Universities for Research in Astronomy, Inc., under cooperative agreement with the National Science Foundation.

emission object and fills the apertures. For such a target, the effective spectral resolution is a combination of the instrumental resolution ($\sim 0.05\text{\AA}$), the slit width, and a further degradation caused by detector astigmatism (Sahnou et al. 2000). The width of the airglow lines in a spectrum is a measure of the effective spectral resolution. In our data, the effective spectral resolutions are $\sim 0.34\text{\AA}$ for the LWRS data and $\sim 0.09\text{\AA}$ for the MDRS data. (These numbers correspond to about 100 km s^{-1} and 30 km s^{-1} , respectively, at 1000\AA .)

The longslit optical spectra presented here were obtained in 1989 February at Las Campanas Observatory. The observations used the du Pont 2.5 m telescope, the Modular Spectrograph and an 800×800 pixel TI CCD. A 600 line mm^{-1} 5000\AA blaze grating was used with an 85 mm camera, providing spectral coverage, $4750 - 7150\text{\AA}$ at 3.0\AA per pixel. The slit width was $2''$ and the effective spectral resolution was 8\AA . The spatial scale along the slit was $0''.8\text{ pixel}^{-1}$, with a usable slit length of $7'$. The slit was placed along the East-West direction, passing through the optical filaments $\sim 1''$ below the slit center of the HUT position P1.

The data were reduced using standard IRAF procedures, including bias subtraction, flat fielding, image rectification and extraction of one dimensional spectra. The background was determined from a portion of the slit lying outside the remnant and subtracted from the spectra. The flux calibration was done using observations of standard stars from the list of Stone & Baldwin (1983). Fiducial stars along the slit, and the known spatial scale were used to extract regions of the long slit data corresponding to the intersection of the slit with the HUT apertures. The optical images (Figure 1b) show that the emission is fairly uniform within the apertures, so the optical spectra should be representative of the overall emission within the HUT apertures at P1 and P2.

3. Discussion

3.1. Optical Imagery and Spectra

The optical narrowband images show a striated emission structure. There are bands of green (strong [O III]), yellow (strong [O III] and $\text{H}\alpha$) and red (strong $\text{H}\alpha$) running parallel to the shock front (Figure 1b), indicating a systematic variation of the $\text{H}\alpha$ to [O III] flux ratio. The $\text{H}\alpha$ emission is at its brightest in the region between about $50''$ and $70''$ behind the leading [O III] edge. The [O III] emission reaches its peak at about the same location as the $\text{H}\alpha$ ($\sim 50''$ behind the edge). In the green ([O III] dominated) band of emission, the [O III] flux is about 40% of its peak value, while the $\text{H}\alpha$ flux remains below 20% of its peak value.

The brightest optical filaments lie approximately parallel to the Southeast edge of the X-ray emitting region (Figure 1a) and there is a gap of about $1'$ between the X-ray edge and the filaments. Observations of other shock-cloud interactions in the Cygnus Loop (Hester & Cox 1986; Danforth et al. 2000) and in Vela (Raymond et al. 1997; Sankrit et al. 2001) have shown that optical filaments are typically coincident with the edges of bright X-ray features, and not separated as in Knot D. So though the association of X-ray and optical regions is expected in SNR shocks, the existence of a gap between the two is surprising.

The optical spectra of the regions of bright and faint $H\alpha$ (P1 and P2, respectively) are shown in Figure 2. We measured the integrated line fluxes using the IRAF task, `splot`, and calculated the surface brightnesses. We derive the color excess from the observed ratio between between the $H\alpha$ and $H\beta$ fluxes. The intrinsic ratio between the two lines for shock excited emission is 3.0 (Raymond 1979). The observed ratio at P1, $I_{H\alpha}/I_{H\beta} \simeq 3.4$, implies that $E_{B-V} = 0.1$, a value consistent with those obtained for other regions in Vela (Wallerstein & Balick 1990). At position P2, we only have an upper limit for the $H\beta$ flux and cannot estimate the color excess. Therefore we assume that the P1 value applies to the whole region. We used the extinction curve suggested by Fitzpatrick (1999), and total to visual selective extinction $R = 3.1$ to calculate correction factors for all the lines. The surface brightnesses of the optical lines, corrected for interstellar extinction are presented in Table 1.

The brightness ratio, $I_{[S II]}/I_{H\alpha}$ is greater than 1 at both positions P1 and P2. The high ratios imply that the gas is collisionally excited and confirm that the optical filaments are due to shocks. As expected from the narrowband images, the optical spectra at the two positions differ significantly in the strength of $[O III]$ emission relative to emission from the lower ionization lines. The $[O III] \lambda\lambda 4959, 5007$ flux is about 3 times weaker at position P2 than at P1, whereas all the other lines are about an order of magnitude weaker at P2. Some lines, including $[O I] \lambda\lambda 6300, 6364$ are not detected at the latter position. This difference suggests that at P2, the shock is “incomplete” - it has not yet swept up enough material for the post-shock gas to have recombined and produced strong $H\alpha$, $[S II]$ and other low ionization lines.

3.2. HUT Spectra

The HUT spectra of the two positions in Knot D contain numerous emission lines expected from SNR shocks (Figure 3). As expected from the *Voyager* UVS spectrum (Blair, Vancura & Long 1995), C III $\lambda 977$ and O VI $\lambda\lambda 1032, 1038$ are the strongest lines below 1200\AA . Other lines such as N III $\lambda 991$, which were lost in the low resolution *Voyager* spectrum, are detected in these HUT data. Longward of 1200\AA , the strongest lines are

C IV $\lambda 1549$, O III] $\lambda 1663$ and N III] $\lambda 1751$. Many (but not all) of the detected lines are marked in Figure 3. One surprise is that N V $\lambda 1240$ is relatively weak: in spectra of radiative shocks in the Cygnus Loop the line is comparable in strength to the C IV line (Blair et al. 1991).

The integrated line fluxes in the spectra were measured using the IRAF tasks `splot` and the more sophisticated `specfit` (Kriss 1994), the latter for blended lines. The pair of lines, Si IV $\lambda 1402$ and O IV] $\lambda 1403$ could not be deblended automatically. Therefore, it was assumed that the Si IV $\lambda 1402$ flux was exactly half the Si IV $\lambda 1394$ flux (valid for optically thin emission). This amount was subtracted from the measured flux of the 1403\AA feature and added to the 1394\AA line. The surface brightnesses of the lines, corrected for interstellar extinction, are listed in Table 2 along with the correction factors. It should be noted that the interstellar extinction curve at wavelengths below 1000\AA is poorly known and is the main source of uncertainties in the intrinsic brightness of the shortest wavelength lines.

The line strengths at P1 are about twice those at P2, but apart from that overall factor the spectra at the two positions are similar. The dramatic differences in the relative intensities of optical lines are not present for the ultraviolet lines. This implies that the shock conditions are similar at the two positions. For instance $I_{\text{O VI}1032,1038}/I_{\text{O III}1664}$, a ratio that is very sensitive to the maximum temperature reached behind the shock, is ~ 1.3 at P1 and ~ 1.2 at P2. Thus the far-ultraviolet spectra support the idea that the difference in the optical emission between P1 and P2 is due to different levels of shock completeness, rather than differences in shock velocity. The main difference between the HUT P1 and P2 spectra is the ratio between the two O VI doublet lines: $I_{1038}/I_{1032} \simeq 0.76$ at P1 and $\simeq 0.61$ at P2. The ratio approaches 0.5 when the line optical depth tends to zero, and approaches 1.0 when the line is optically thick. The measured ratios show that the line fluxes are affected by resonance line scattering and that the effect is stronger at P1 than at P2.

The ratio between the O VI line fluxes can be affected by absorption of the 1038\AA line by molecular hydrogen (the Lyman band transitions, $R(1)_{5-0}$ and $P(1)_{5-0}$, at 1037.15\AA and 1038.16\AA , respectively) and by C II* (1037.02\AA). The ratio can also be affected by self-absorption of the lines by O VI in the ISM. Jenkins, Silk & Wallerstein (1976) find the column of low velocity H_2 in the $J=1$ state $N_{J=1} \simeq 10^{14.5}$, $10^{15.5}$, and $10^{17.8}$ towards three stars behind Vela. Even the highest of these would absorb only about 9% of the flux from a 150 km s^{-1} width line centered at zero velocity. The more typical lower values for the column would have negligible effect on the O VI $\lambda 1038$ flux. The C II* line is stronger, but is at -173 km s^{-1} relative to the O VI $\lambda 1038$ rest wavelength. The velocity profile of the O VI lines in the FUSE LWRS spectrum (see below) shows that C II* absorption would not reduce the O VI flux significantly. The O VI column out to the distance of Vela (250 pc)

is $\sim 10^{13} \text{ cm}^{-2}$ (Jenkins et al. 2001), which would have negligible affect on the line fluxes. Also, Knot D lies beyond the remnant boundary, and it is unlikely that other shocked clouds associated with Vela lie in front of it. Therefore, the ratios measured in the HUT spectra should not be modified significantly by foreground absorption.

3.3. FUSE Spectra

3.3.1. LWRS Spectrum

The FUSE LWRS spectrum is shown in Figure 4. The strongest SNR lines in the FUSE bandpass are C III $\lambda 977$ and O VI $\lambda\lambda 1032, 1038$. These lines are allowed to go off-scale in the plot in order to show a number of the weaker lines present in the spectrum. The weak lines are well separated from each other and are easily identified. Furthermore, SNR lines can be distinguished from airglow lines by comparing the total spectrum with a spectrum screened to include only orbital night data. Many of these weaker lines have been detected in SNR spectra for the first time by FUSE. For example, this paper reports the first such detection of S III $\lambda 1077$. Note that the region around He II+[N II] $\lambda 1085$ is not included in the plots. This range lies at the edge of only one detector segment (Sahnow et al. 2000), and the telescope effective area is very small in this region.

The total line fluxes in the LWRS spectrum were obtained by trapezoidal integration of the flux vector with suitable background subtraction. The strong lines contain several thousand counts, so the random errors in their measured fluxes are low ($\sim 1\%$). The errors are about 6% for some of the weaker lines, such as S III $\lambda 1015$ and S IV $\lambda 1063$. For the weakest line fluxes, particularly those detected in the SiC 2A segment (e.g. S VI $\lambda\lambda 933, 944$), uncertainties in the background placement contribute to the total error, which is about 20%. The uncertainty in the absolute flux calibration is about 10% (Sahnow et al. 2000), which dominates the statistical errors in the measured fluxes of the strong lines and is comparable to those of the weak lines. The surface brightnesses of the lines, corrected for interstellar extinction, are presented in Table 3.

The fluxes of the strong lines (C III and O VI) plotted on a velocity scale are shown in Figure 5. (The velocity is relative to the Local Standard of Rest, in which frame the sun is moving away from Vela at about 12.5 km s^{-1} .) The top panel is an overlay of the two O VI lines. The lines are centered at $\sim +18 \text{ km s}^{-1}$ and the FWHM of each line is $\sim 130 \text{ km s}^{-1}$. If the emission fills the slit uniformly, then the observed line profile is the intrinsic profile convolved with the line spread function, which, to very good approximation, is a 106 km s^{-1} wide “tophat” function. Under this assumption the O VI lines have intrinsic FWHMs of

$\sim 100 \text{ km s}^{-1}$. The surface brightnesses of the O VI in the FUSE LWRS spectrum lies between the HUT P1 and P2 values (Tables 2, 3). However, the ratio $I_{1038}/I_{1032} \simeq 0.58$ in the FUSE LWRS spectrum, which is lower than the value at either HUT position. Thus, when detected over the more spatially extended LWRS aperture, resonance scattering has a smaller effect on the O VI emission than when detected over the HUT aperture at P1 or P2.

The feature on the blue wing of O VI $\lambda 1038$ is identified as C II $\lambda 1037.02$, a line also detected in a FUSE spectrum of an X-ray bright knot in the center of Vela (Sankrit et al. 2001). The transition leading to the 1037.02\AA line has a lower state 63 cm^{-1} above the ground state. The companion line, C II $\lambda 1036.34$ is a strong ground state transition (Morton 1991) and is not detected because it is absorbed by the interstellar gas between us and the SNR.

The bottom panel of Figure 5 shows an overlay of the C III and the O VI $\lambda 1032$ lines. The C III line is significantly broader than the O VI line, and it has a central reversal. By fitting the wings of the C III profile with gaussians we find that the observed peaks are centered at $\sim -60 \text{ km s}^{-1}$ and $\sim +80 \text{ km s}^{-1}$, and that the components have FWHMs $\sim 100 \text{ km s}^{-1}$. C III is a strong resonance line, and while the observed profile is consistent with there being two kinematic components, we expect optical depth effects to influence the line profile. Some idea about the intrinsic velocity distribution of low ionization emission is gleaned from the [S II] $\lambda 6716$ position-velocity data presented by Redman et al. (2000). In an echelle spectrum with the slit cutting across the optical filament about $2'$ south of the FUSE LWRS position, Redman et al. (2000) detected bright [S II] emission around zero-velocity. In addition to this central component, they found fainter red-shifted and blue-shifted peaks (see their Figure 4). The intrinsic velocity structure of the C III emission is likely to be as complex, in which case the reversal in the observed profile is due to zero-velocity emission being self-absorbed by both filament material and the ISM along the sightline.

3.3.2. MDRS Spectrum

C III $\lambda 977$ and the O VI doublet are detected in the FUSE MDRS spectrum, obtained at a position several arcminutes behind the bright optical filaments. The line fluxes are plotted against LSR velocity in Figure 6. The two O VI lines track each other closely (Figure 6 top panel). Each O VI line profile has two peaks, centered at $\sim -80 \text{ km s}^{-1}$ and $\sim +80 \text{ km s}^{-1}$. The width of the gap between the two components is about 90 km s^{-1} , which is much greater than the typical velocity width $\sim 40 \text{ km s}^{-1}$ for absorption by interstellar O VI (Jenkins et al. 2001). We conclude that we are seeing two distinct emitting components (rather than a single, self-absorbed component) along the line of sight at this location. The

kinematic structure of the C III emission follows that of the O VI emission (Figure 6 bottom panel). The C III line has two peaks, centered at the same velocities as the O VI lines. The separation between the two C III velocity components is larger in the the MDRS spectrum than in the LWRS spectrum. Because of its bow shape, and because of the lack of complex optical morphology at the location of the MDRS aperture (Figure 1), we conclude that the two emission components are due to shocks on the front and back sides of Knot D. The blue-shifted O VI lines have FWHMs of about 70 km s^{-1} , and are broader than their red-shifted counterparts, which are about 50 km s^{-1} wide (FWHM). Both C III components have FWHMs of about 50 km s^{-1} .

The surface brightnesses, corrected for interstellar extinction, of the blue and red shifted components of the three lines are presented in Table 4. The blue shifted component of C III $\lambda 977$ is about 1.3 times as bright as the red shifted component. In contrast, the total O VI flux of the blue shifted component is just half that of the red shifted component. $I_{\text{O VI}}/I_{\text{C III}}$ is about 0.9 for the red shifted component and about 0.4 for the blue shifted component. The ratios between the doublet lines, I_{1038}/I_{1032} are 0.54 for the blue shifted component and 0.56 for the red shifted component. These ratios are closer to the optically thin limit compared with the values obtained for the HUT and FUSE LWRS spectra, which is consistent with the less edge-on viewing geometry expected at this position.

4. Analysis and Interpretation

4.1. Shock Models

To facilitate interpretation of the ultraviolet spectra, we compare the data with shock model calculations. We focus on the bright filament covered by the HUT P1 and FUSE LWRS apertures, and generate a list of line strengths relative to $I_{\text{O III]}} = 100$. The two apertures cover different regions on the sky, and the O VI surface brightness is lower in the FUSE LWRS spectrum. We use the O VI to O III] line ratio measured in the HUT P1 spectrum. The line strengths of other high ionization lines below 1200\AA , S VI, Ne VI] and Ne V], are scaled relative to $I_{\text{O VI}}$ based on the FUSE LWRS measurement, and then rescaled relative to $I_{\text{O III]}}$ based on the HUT P1 O VI to O III] line ratio. The FUSE LWRS surface brightnesses are used for all other lines in the FUSE bandpass. These data are shown in column 3 of Table 5.

Shock models were calculated using an updated version of the code presented by Raymond (1979). The updates are discussed by Raymond et al. (1997), and some atomic rates for Si III, Si IV and S IV lines have been updated based on the CHIANTI database (Dere et

al. 2001). The model follows the emission and cooling behind a steady shock moving into a constant density medium. The main inputs are the shock velocity, the pre-shock density and the elemental abundances. Models are presented for a range of shock velocities. In each case the pre-shock hydrogen number density, n_0 is 1 cm^{-3} . (The ultraviolet line fluxes scale linearly with pre-shock density so model line ratios do not depend on n_0 .) Elemental abundances, H : He : C : N : O : Ne : Mg : Si : S : Ar : Ca : Fe : Ni = 12.00 : 11.00 : 8.55 : 7.97 : 8.79 : 8.07 : 7.58 : 7.55 : 7.21 : 6.60 : 6.36 : 7.51 : 6.25 on a logarithmic scale, are used in the models. Except for the Oxygen abundance (discussed below) these are solar abundances based on Grevesse & Anders (1989) and tabulated by Ferland (1997). In all the models the pre-shock magnetic field is $1 \mu\text{G}$, the temperature of the pre-shock gas 10,000 K, and the gas is fully ionized. These parameters do not affect the ultraviolet line strengths significantly. For each model, the calculation is followed until the post-shock gas reaches about 1000 K, by which point the recombination zone is complete.

The ratio of N III] $\lambda 1750$ to O III] $\lambda 1664$ is relatively insensitive to the shock velocity. For the range of shock velocities between about 80 km s^{-1} and 120 km s^{-1} , the ratio is a measure of the relative abundances of Nitrogen and Oxygen. There is some amount of uncertainty in the value for solar oxygen abundance. Ferland (1997), from which we have taken the other abundances, lists $[\text{O}] = 8.87$. Recently, it has been suggested that the actual value is lower than normally assumed: Holweger (2001) gives $[\text{O}] = 8.73$, and Allende Prieto, Lambert, & Asplund (2001) give $[\text{O}] = 8.69$. We ran a set of 100 km s^{-1} shock models varying the oxygen abundance between 8.69 and 8.87 (and keeping other abundances fixed). The observed N III] to O III] line ratio is obtained for Oxygen abundance, $[\text{O}] = 8.79$, and we used this value in the models presented in columns 4–9 of Table 5.

The optical depths of the strongest resonance lines observed are of order unity in the direction normal to the shock front. When viewed close to edge-on (as expected at and near P1), the optical depths are higher. A significant fraction of the line photons emitted by the shocked gas are scattered out of the line of sight, reducing the observed fluxes. While comparing spectra with shock model predictions, it is necessary to take into consideration this decrease in fluxes due to resonance line scattering.

In the case of the O VI lines, the ratio between the intensities of the two lines of the doublet is a measure of the line optical depth. If we assume that the optical depth along the line of sight is much higher than the transverse optical depth then, as described by Long et al. (1992), we can calculate the intensity correction factor. For an observed ratio $I_{1038}/I_{1032} \simeq 0.76$, the intensity correction factor is ~ 2.14 (for the sum of both lines). The carbon lines, C III $\lambda 977$, C II $\lambda 1335$ and C IV $\lambda 1549$ are all significantly affected by resonance scattering. The flux ratio between C III $\lambda 977$ and C III $\lambda 1176$ provides an estimate of the

effects of resonance scattering on the 977Å line. The models predict a ratio of about 80, while the observed ratio is about 20, indicating a correction factor of about 4. This conclusion is somewhat compromised because of uncertainties in the model predictions of the 1176Å line. We expect that N V λ 1240 flux is less affected by resonance scattering than any of these other lines because nitrogen is less abundant. Specifically, we may assume that the correction factor for the 1240Å line (actually an unresolved doublet) is not more than the correction factor for the O VI doublet derived above.

4.2. Shock Properties

The ultraviolet spectrum provides several diagnostic line ratios that can be used to estimate the shock velocities. The ratios N IV] λ 1490 to N III] λ 1750 and O IV] λ 1403 to O III] λ 1604 are particularly useful: the lines are intercombination lines and so are not subject to optical depth effects, and the ratios do not depend on abundances. At the HUT P1 position, $I_{\text{N IV]}}/I_{\text{N III]}} \sim 0.32$ and $I_{\text{O IV]}}/I_{\text{O III]}} \sim 0.44$. A shock velocity $v_s \lesssim 100 \text{ km s}^{-1}$ is required to reproduce these observed values. It is clear from Table 5 that such a low velocity shock cannot produce the observed flux of higher ionization lines such as N V λ 1240 and the O VI doublet. If we assume that both N V and O VI are equally affected by resonance scattering then $I_{\text{O VI}}/I_{\text{N V}} \sim 7.5$. To produce this ratio requires a shock velocity of about 170 km s^{-1} . If N V is less affected by resonance scattering, then the ratio is higher and so is the required shock velocity. The ratio between Ne VI] λ 1006 and Ne V] λ 1146 is less accurate because the lines are weak, but these lines are not affected by resonance scattering, and the observed ratio implies shock velocities in excess of 180 km s^{-1} . Finally, we note that the ratio of optical lines $I_{[\text{O III]}}/I_{[\text{S III]}} \sim 3.1$ (Table 1), which requires shock velocities of at least 80 km s^{-1} . (The forbidden line strengths are predicted by shock models but are not presented in Table 5.)

From these comparisons we find that the lower ionization lines, including O III], O IV], N III] and N IV], come predominantly from shocks with velocities $\lesssim 100 \text{ km s}^{-1}$ and the higher ionization lines such as O VI, N V, S VI, Ne V] and Ne VI] come from faster shocks, with velocities about 180 km s^{-1} . The latter velocity falls within the range given by Blair, Vancura & Long (1995) for O VI producing shocks, but our value for the velocity of the slower shock is less than their estimate for the C III producing shocks (see §1). Intermediate velocity shocks cannot contribute a significant fraction of the emission since that would affect all the line ratios in the wrong way. For example, if there were a substantial contribution from say a 140 km s^{-1} shock, then $I_{\text{N IV]}}/I_{\text{N III]}}$ would be higher than observed while $I_{\text{O VI}}/I_{\text{N V}}$ would be lower than observed. The lack of correlation between the C III and O VI velocity

distributions in the FUSE LWRS spectrum (Figure 5) provides corroborating evidence that the two lines arise in different shocks. Since the ultraviolet line ratios are similar in both HUT spectra (§3.2), the arguments and conclusions presented above for P1 also hold for P2.

The observed O III] $\lambda 1664$ surface brightness, $I_{obs} = 3.1 \times 10^{-15} \text{ erg s}^{-1} \text{ cm}^{-2} \text{ arcsec}^{-2}$ (Table 2). To proceed with our analysis, we make the simplifying assumption that a 100 km s^{-1} shock is responsible for all the O III] emission. A 100 km s^{-1} shock model using a pre-shock hydrogen number density $n_{mod} = 1 \text{ cm}^{-3}$ predicts an O III] line intensity $4.5 \times 10^{-6}/2\pi \text{ erg s}^{-1} \text{ cm}^{-2} \text{ sr}^{-1}$ (Table 5). This is equivalent to $I_{mod} = 1.7 \times 10^{-17} \text{ erg s}^{-1} \text{ cm}^{-2} \text{ arcsec}^{-2}$. The model prediction scales with the pre-shock density. Also the model predicts the intensity emerging perpendicular to the shock front. Since the shock front is viewed close to edge-on, the effective area of the shock observed is larger than the aperture area. The $56'' \times 10''$ HUT aperture is placed parallel to the shock front. If the path length through the O III] emitting gas is l'' , then the ratio of the shock area to aperture area is $l/10$. Thus, $I_{obs} = n_{100} \times I_{mod} \times l/10$, where n_{100} is the pre-shock density for the 100 km s^{-1} shock component. Substituting the values for observed and model surface brightnesses, we obtain: $n_{100} \times l \simeq 1800$.

Below we find that the dynamic pressure of the shocks observed at the FUSE MDRS position, $\rho_0 v_{shock}^2 \simeq 2.6 \times 10^{-9} \text{ dyne cm}^{-2}$. Assuming that this is the pressure driving the shocks at P1, for $v_{shock} = 100 \text{ km s}^{-1}$ and $[\text{He}] = 11.0$, we obtain $n_{100} \simeq 11 \text{ cm}^{-3}$. This, in turn, implies that the path length through the emitting gas is about $164''$, which is about 0.2 pc at the distance of Vela. The length of the optical filament in the plane of the sky is about $430''$, which is significantly higher than the derived path length through the O III] emitting gas. The difference is probably due to the curvature of the shock front into the plane of the sky, but could also be because the cloud that the shock is running into is approximately cylindrical with its long direction oriented in the plane of the sky. As we showed above, the high ionization lines are produced by faster shocks. For a 180 km s^{-1} shock, the isobaric condition yields a pre-shock density $n_{100} \times (100/180)^2 \sim 3.5 \text{ cm}^{-3}$.

At the FUSE MDRS position, the observed O VI to C III ratios are 0.4 for the blue-shifted component and 0.9 for the red-shifted component (Table 4). (Note: no correction for resonance scattering was made in this case.) We ran a set of shock models with velocities in the range $140\text{--}160 \text{ km s}^{-1}$ spaced by 5 km s^{-1} . By interpolating from the predicted line ratios we found that the observed values for the blue-shifted and red-shifted components are satisfied for shock velocities of $\sim 151 \text{ km s}^{-1}$ and $\sim 157 \text{ km s}^{-1}$, respectively. We note for shock velocities from 140 to 160 km s^{-1} that $I_{O\text{ VI}}$ increases rapidly while $I_{C\text{ III}}$ stays fairly constant (Table 5).

If our line of sight intersects with a shock front once, then the following holds (Raymond

et al. 1997): $I_0 = I_{obs}v_{obs}/v_{shock}$, where I_0 is the intensity of the shock viewed face-on, v_{obs} is the observed radial velocity (absolute value) and v_{shock} is the shock velocity. We apply this to the C III emission. The observed surface brightnesses are 21.8×10^{-16} and 16.8×10^{-16} erg s⁻¹ cm⁻² arcsec⁻² for the blue- and red-shifted components (Table 4). The central velocities of the components are ~ -80 km s⁻¹ and $\sim +80$ km s⁻¹. Using these values in the equation above yields $I_0(blue) \approx I_0(red) \simeq 1 \times 10^{-15}$ erg s⁻¹ cm⁻² arcsec⁻². The face-on C III intensity predicted by a 150 km s⁻¹ shock model for pre-shock density 1.0 cm⁻³, $I_{mod}(C\ III) \simeq 2 \times 10^{-16}$ erg s⁻¹ cm⁻² arcsec⁻². The line intensity scales with pre-shock density, so the pre-shock density required to produce the observed C III brightness is $I_0/I_{mod}(C\ III) \sim 5$ cm⁻³. Using the values for shock velocity and pre-shock density derived above, we find that the pressure in the X-ray knot driving the shock ($P = \rho_0 v_{shock}^2$) is about 2.6×10^{-9} dyne cm⁻² ($P/k_B \sim 1.8 \times 10^7$ cm⁻³ K).

The dynamical pressure of the shock derived above is about twice the value derived from the HUT spectrum of a face-on shock near the center of the remnant (Raymond et al. 1997), and about seven times the value in the X-ray region associated with the face-on shock (Sankrit et al. 2001). It is also about 25 times the characteristic pressure of the X-ray emitting gas derived by Kahn et al. (1985), corrected for the revised distance of 250 pc to Vela. The high pressure is consistent with Knot D originating in a bullet near the center of the remnant in that the bullets have to have ram pressures substantially larger than the average to punch out through the shell. The enhanced pressure would not be consistent with the knot being a blister on the surface, such as formed in the model suggested by Meaburn, Hartquist & Dyson (1988) for expanding SNR shells. It is interesting that Jenkins & Wallerstein (1995) derived a pressure slightly higher than our value in the region around the line of sight towards HD 72089, which is also near some arcuate optical filaments. They also found several high velocity components in the absorption spectrum of the star. The enhanced pressure suggests that the high velocity emission and optical filaments at the position observed by Jenkins & Wallerstein (1995) may be related to a bullet similar to Knot D but traveling towards us.

We have used steady flow shock models to explain the observed emission lines. At the MDRS location, these lines arise in a shell within the surface of an evolving bow shock. Hartigan, Raymond & Hartmann (1987) approximate a Herbig-Haro bow shock by a series of plane parallel, steady flow oblique shocks; an approximation that they find valid if the cooling time is short compared to dynamical times. Knot D is about 30' (6.7×10^{18} cm) beyond the main blast wave. Assuming that it is moving at ~ 500 km s⁻¹ (Aschenbach, Egger & Trümper 1995), it has taken about 4000 years for it to get to its current position since overtaking the blast wave. The cooling time for a 150 km s⁻¹ shock running into 5 cm⁻³ material is about 300 years. The front of the bow shock is running into a denser part of the

cloud. This encounter results in a slower shock that gives rise to the optical filaments as also the low ionization ultraviolet lines.

The use of steady flow models has another limitation: shocks of 180 km s^{-1} are subject to thermal instabilities (e.g. Chevalier & Imamura 1982). The structure and spectrum of such a shock fluctuate in time (Innes, Giddings & Falle 1987; Gaetz, Edgar & Chevalier 1988), but the spectrum averaged over time is not greatly affected (Innes 1992). The spectrograph apertures include emission from sufficiently complex filaments that the fluctuations are probably smoothed out.

5. Concluding Remarks

We have analyzed far-ultraviolet and optical observations of Knot D in the Vela SNR, and shown that the emission is due to shocks driven into a medium with typical interstellar cloud densities and normal elemental abundances. We have also found that the dynamical pressure of the shocks is higher than the characteristic value for the remnant. We have estimated that the path length through the optical filaments is shorter than their extent in the plane of the sky implying a curved shock front. The velocity profiles of the lines revealed by high resolution FUSE MDRS is consistent with emission from a bow shock. The over-pressure in Knot D supports the idea that it is a bow shock around a bullet or cloud that originated near the center of the remnant and has punched through the shell. However, there is no evidence for enhanced abundances. If the driver of the bow shock is a shrapnel of ejecta (Aschenbach, Egger & Trümper 1995), then it remains undetected. An alternative candidate for the driver is an accelerated cloud that originated near the center. The existence of such clouds was suggested by McKee, Cowie & Ostriker (1978) to explain some of the high velocity emission observed in SNRs.

Knot D, in spite of its unique properties, may be one of many such features including the ones observed in the plane of the sky around Vela, as well as others moving radially towards or away from us. In any case, our study provides an estimate of the properties of Knot D that can be usefully compared with results derived from X-ray data. The properties of Knot D can also be compared with those of other regions to find out the extent of their similarities.

The suggestion that Knot D is associated with RXJ0852.0-4622 (Redman et al. 2002) has been made mainly on morphological grounds. The connection also depends on the smaller remnant being at about the same distance as the Vela SNR. The distance and also the age of RXJ0852.0-4622 are highly uncertain (Duncan & Green 2000) and provide

very few constraints on the properties of putative blow-out regions. We have found that the interstellar extinction towards the optical filaments is typical for the Vela SNR. Furthermore our ultraviolet data do not show any peculiarities (e.g. in the velocity distribution) that suggest a connection between the knot and the newly discovered remnant. Therefore, we believe that Knot D is associated with the Vela SNR. It will require additional studies to prove or disprove conclusively the association between RXJ0852.0-4622 and Knot D.

One major issue that remains unanswered is the gap of about $1'$ between the optical filaments and the edge of the X-ray knot (Figure 1). This is not seen in typical shock-cloud interactions (see references in §3.1) where the X-ray edge and optical emission are co-incident. In those cases, the relationship of the two components is well explained by a model in which the blast wave hits the cloud and a reverse shock is propagated back into the remnant (Graham et al. 1995). In Knot D, the gap must be a consequence of the dynamics of the bow shock. The gap region could contain gas that is hot but with a temperature not high enough to make X-rays. The region may then be a source of bright O VI emission. It could also be a transient region of low pressure as predicted by models of thermal instability (Innes 1992). A third possibility is that it is a region of cool gas supported by magnetic pressure. Each of these possibilities has interesting implications for the structure and evolution of astrophysical bow shocks, but the existing data do not allow us to distinguish among them. However, it is worth noting that the spatial extent of the gap may be related to the cooling length of the shocked gas. At the distance of Vela, $1'$ is about 2×10^{17} cm, which is roughly the cooling length scale of a 240 km s^{-1} shock in a medium with density 3 cm^{-3} . These conditions may have obtained in the course of the evolution of the bow shock. Detailed models and direct observations are needed for further elucidation.

We thank Paul Plucinsky for useful discussions, and for providing us with the Chandra image presented in Figure 1. We also thank Matt Redman for giving us access to his [S II] position-velocity data. H2ools, a software package written by Steve McCandliss was used in estimating the effects of molecular hydrogen absorption. The referee’s comments helped improve the flow and focus of the paper. This work has been supported by NASA grant NAG5-10248 and NASA contract NAS5-32985, both to the Johns Hopkins University.

REFERENCES

- Allende Prieto, C., Lambert, D. L., & Asplund, M 2001, ApJ, 556, L63
- Aschenbach, B. 1998, Nature, 396, 141
- Aschenbach, B., Egger, R., & Trümper, J. 1995, Nature, 373, 587
- Blair, W. P. et al. 1991, ApJ, 379, L33
- Blair, W. P., Vancura, O, & Long, K. S. 1995, AJ, 110, 312
- Cha, A. N, Sembach, K. R., & Danks, A. C. 1999, ApJ, 515, L25
- Chevalier, R. A., & Imamura, J. N. 1982, ApJ, 261, 543
- Danforth, C. W., Cornett, R. H., Levenson, N. A., Blair, W. P., & Stecher, T. P. 2000, AJ, 119, 2319
- Davidson, A. F. et al. 1992, ApJ, 392, 264
- Dere, K. P., Landi, E., Young, P. R., & Del Zanna, G. 2001, ApJS, 134, 331
- Dubner, G. M., Green, A. J., Goss, W. M., Bock, D. C.-J., & Giacani, E. 1998, AJ, 116, 813
- Duncan, A. R., & Green, D. A. 2000, A&A, 364, 732
- Ferland, G. J. 1997, Hazy I, a brief introduction to Cloudy 90, pg. 50
- Fitzpatrick, E. L. 1999, PASP, 111, 63
- Gaetz, T. J., Edgar, R. J, & Chevalier, R. A. 1988, ApJ, 329, 927
- Graham, J. R., Levenson, N. A., Hester, J. J., Raymond, J. C., & Petre, R. 1995, ApJ, 444, 787
- Grevesse, N., & Anders, E. 1989, Cosmic Abundances of Matter, AIP Conf. Proc. 183, 1 Ed. C. J. Waddington (New York : AIP)
- Hartigan, P., Raymond, J., & Hartmann, L. 1987, ApJ, 316, 323
- Hester, J. J., & Cox, D. P. 1986, ApJ, 300, 675
- Holweger, H. 2001, Solar and Galactic Composition, Ed. R. F. Wimmer-Schweingruber (Melville, NY: AIP), p. 23

- Innes, D. E. 1992, *A&A*, 256, 660
- Innes, D. E., Giddings, J. R., & Falle, S. A. E. G. 1987, *MNRAS*, 226, 67
- Jenkins, E. B., Bowen, D. V., Sembach, K. R., & the FUSE Science Team 2001, *astro-ph*, 0109363
- Jenkins, E. B., Silk, J., & Wallerstein, G. 1976, *ApJS*, 32, 681
- Jenkins, E. B., & Wallerstein, G. 1995, *ApJ*, 440, 227
- Kahn, S. M., Gorenstein, P., Harnden, F. R., & Seward, F. D. 1985, *ApJ*, 299, 821
- Kriss, G. A. 1994, in *ADASS III*, ASP Conf. Proc. 61, ed. D. R. Crabtree, R. J. Hanisch, & J. Barnes (San Francisco: ASP), 437
- Kruk, J. W., Durrance, S. T., Kriss, G. A., Davidsen, A. F., Blair, W. P., Espey, B. R., & Finley, D. S. 1995, *ApJ*, 454, L1
- Kruk, J. W., Brown, T. A., Davidsen, A. F., Espey, B. R., Finley, D. S., & Kriss, G. A. 1999, *ApJS*, 122, 299
- Long, K. S., Blair, W. P., Vancura, O., Bowers, C. W., Davidsen, A. F., & Raymond, J. C. 1992, *ApJ*, 400, 214
- McKee, C. F., Cowie, L. L., & Ostriker, J. P. 1978, *ApJ*, 219, L23
- Meaburn, J., Hartquist, T. W., & Dyson, J. E. 1988, *MNRAS*, 230, 243
- Moos, H. W., et al. 2000, *ApJ*, 538, L1
- Moriguchi, Y., Yamaguchi, N., Onishi, T., Mizuno, A., & Fukui, Y. 2001, *PASJ*, 53, 1025
- Morton, D. C. 1991, *ApJS*, 77, 119
- Plucinsky, P. P., Smith, R. K., Edgar, R. J., Gaetz, T. J., Slane, P. O., Blair, W. P., Townsley, L. K., & Broos, P. S. 2002, *ASP Conf. Ser. 271: Neutron Stars in Supernova Remnants*, 407
- Raymond, J. C. 1979, *ApJS*, 39, 1
- Raymond, J. C., Blair, W. P., Long, K. S., Vancura, O., Edgar, R. J., Morse, J., Hartigan, P., & Sanders, W. T. 1997, *ApJ*, 482, 881

- Redman, M. P., Meaburn, J., O'Connor, J. A., Holloway, A. J., & Bryce, M. 2000, *ApJ*, 543, L153
- Redman, M. P., Meaburn, J., Bryce, M., Harman, D. J., & O'Brien, T. J. 2002, *MNRAS*, in press
- Rodgers, A. W., Campbell, C. T., & Whiteoak, J. B. 1960, *MNRAS*, 230, 243
- Sahnou, D. J., et al. 2000, *ApJ*, 538, L7
- Sankrit, R., Shelton, R. L., Blair, W. P., Sembach, K. R., & Jenkins, E. B. 2001, *ApJ*, 549, 416
- Stone, R. P. S., & Baldwin, J. A. 1983, *MNRAS*, 204, 347
- Wallerstein, G., & Balick, B. 1990, *MNRAS*, 245, 701

Fig. 1.— (a) Three color image of the southern part of Knot D. Narrowband $H\alpha$ and [O III] are shown in red and green, respectively. A Chandra ACIS-1 image (courtesy P. Plucinsky) is shown in blue. The FUSE LWRS ($30'' \times 30''$) aperture lies on the optical filament while the MDRS ($4'' \times 20''$) aperture lies on an X-ray bright region ~ 3.5 away. (b) Blow-up of the $H\alpha$ and [O III] images showing the bright optical filaments. The HUT aperture positions and the FUSE LWRS position are shown as white boxes. North is up and East to the left in both images. The LWRS aperture is $30'' \times 30''$.

Fig. 2.— Optical spectra of the filaments at positions P1 and P2. Spatial extractions from a longslit spectrum of regions overlapping the HUT aperture positions were used to obtain these spectra (see text for details). There are no lines observed between 5100\AA and 6200\AA , so that region is not shown in these plots.

Fig. 3.— HUT spectra of the filaments at position 1 (top panel) and position 2 (bottom panel). Note the difference in the range of the y-axis scale between the two plots. The aperture positions are shown in Figure 1.

Fig. 4.— FUSE LWRS spectrum of the filament: the top, middle and bottom panels show data from the SiC 2A, LiF 1A and LiF 2A channels, respectively. The flux range has been chosen to show the weaker lines, and all data have been binned by 12 pixels ($\sim 0.07\text{\AA}$) along the wavelength axis.

Fig. 5.— Fluxes of strong lines observed in the FUSE LWRS spectrum, plotted against velocity. Top panel: overlay of the two O VI lines. The excess emission seen on the blue wing of the 1037\AA line is identified as C II $\lambda 1037$ emission (see text for details). Bottom panel: overlay of O VI $\lambda 1032$ and C III $\lambda 977$.

Fig. 6.— Fluxes of lines observed in the FUSE MDRS spectrum, plotted against velocity. Top panel: overlay of the two O VI lines. Bottom panel: overlay of O VI $\lambda 1032$ and C III $\lambda 977$.

Table 1. Optical Surface Brightnesses at HUT P1 and P2

Line ID	$\lambda(\text{\AA})$	SB(P1)	SB(P2)	Red. Corr.
H β	4861	9.1	<1.0	1.40
[O III]	4959	25.9	9.2	1.38
[Fe III]	4987	2.4	...	1.38
[O III]	5007	80.7	28.7	1.38
[Fe II]+Fe[III]	5270	0.9	...	1.35
[N II]	5754	1.2	...	1.30
He I	5876	0.7	...	1.29
[O I]	6300	2.6	...	1.26
[O I]	6364	0.9	...	1.26
[N II]	6548	8.4	0.7	1.24
H α	6563	27.5	2.7	1.24
[N II]	6583	26.5	2.3	1.24
[S II]	6716	19.7	2.5	1.23
[S II]	6731	14.6	1.5	1.23

Note. — Surface brightness units: 10^{-16} erg s $^{-1}$ cm $^{-2}$ arcsec $^{-2}$. Measured fluxes were divided by the area of overlap between the longslit and the HUT aperture positions ($2'' \times 10''$) and corrected for interstellar extinction. The correction factors are presented in the last column of the table.

Table 2. Ultraviolet Surface Brightnesses measured by HUT

Line ID	$\lambda(\text{\AA})$	SB(P1)	SB(P2)	Red. Corr.
S VI	933	3.6	3.1	5.38
S VI	944	2.9	2.5	5.12
C III	977	42.4	19.7	4.47
N III	991	15.6	7.8	4.25
O VI	1032	22.5	10.0	3.73
O VI	1038	17.0	6.1	3.66
S IV	1064	1.8	0.7	3.42
S IV	1074	2.6	1.6	3.34
He II+[N II]	1085	4.5	1.6	3.25
[Ne V]	1146	1.3	...	2.88
C III	1176	2.6	1.4	2.74
N V	1240	5.2	3.4	2.52
C II	1335	4.5	2.2	2.30
O V	1371	<0.7	<0.6	2.24
Si IV	1393	9.3	4.7	2.21
O IV]	1403	13.7	9.1	2.20
N IV]+[N IV]	1485	3.9	3.0	2.11
C IV	1549	26.4	15.2	2.07
[Ne IV]	1602	0.8	1.2	2.04
He II	1640	11.4	3.7	2.03
O III]	1664	31.1	13.8	2.03
N III]	1750	12.8	5.5	2.02

Note. — Surface brightness units: 10^{-16} erg s $^{-1}$ cm $^{-2}$ arcsec $^{-2}$. Measured fluxes were divided by the HUT aperture area ($10'' \times 56''$) and corrected for interstellar extinction. The correction factors are presented in the last column of the table.

Table 3. Surface Brightnesses in the FUSE LWRS Spectrum

Line ID	$\lambda(\text{\AA})$	SB
S VI	933	1.6
S VI	944	1.0
C III	977	40.6
N III	991	11.1
Ne VI	1006	0.8
S III	1015	0.7
S III	1021	0.9
O VI	1032	17.6
O VI	1038	10.3
S IV	1063	2.2
S IV	1074	1.9
S III	1077	0.6
Si III	1110	0.3
Si III	1113	0.4
Si IV	1123	0.3
Si IV	1128	0.6
Ne V	1137	0.2
Ne V	1146	0.5
C III	1176	1.8

Note. — Surface Brightness units: 10^{-16} erg s $^{-1}$ cm $^{-2}$ arcsec $^{-2}$. Measured fluxes were divided by the LWRS aperture area ($30'' \times 30''$) and corrected for interstellar extinction. The correction factors are presented in Table 2.

Table 4. Surface Brightnesses in the FUSE MDRS Spectrum

Line ID	$\lambda(\text{\AA})$	SB (blue)	SB (red)
C III	977	21.8	16.8
O VI	1032	5.1	9.8
O VI	1038	2.8	5.5

Note. — Surface brightness units: 10^{-16} erg s $^{-1}$ cm $^{-2}$ arcsec $^{-2}$. Measured fluxes were divided by the MDRS aperture area ($4'' \times 20''$) and corrected for interstellar extinction. The correction factors are presented in Table 2.

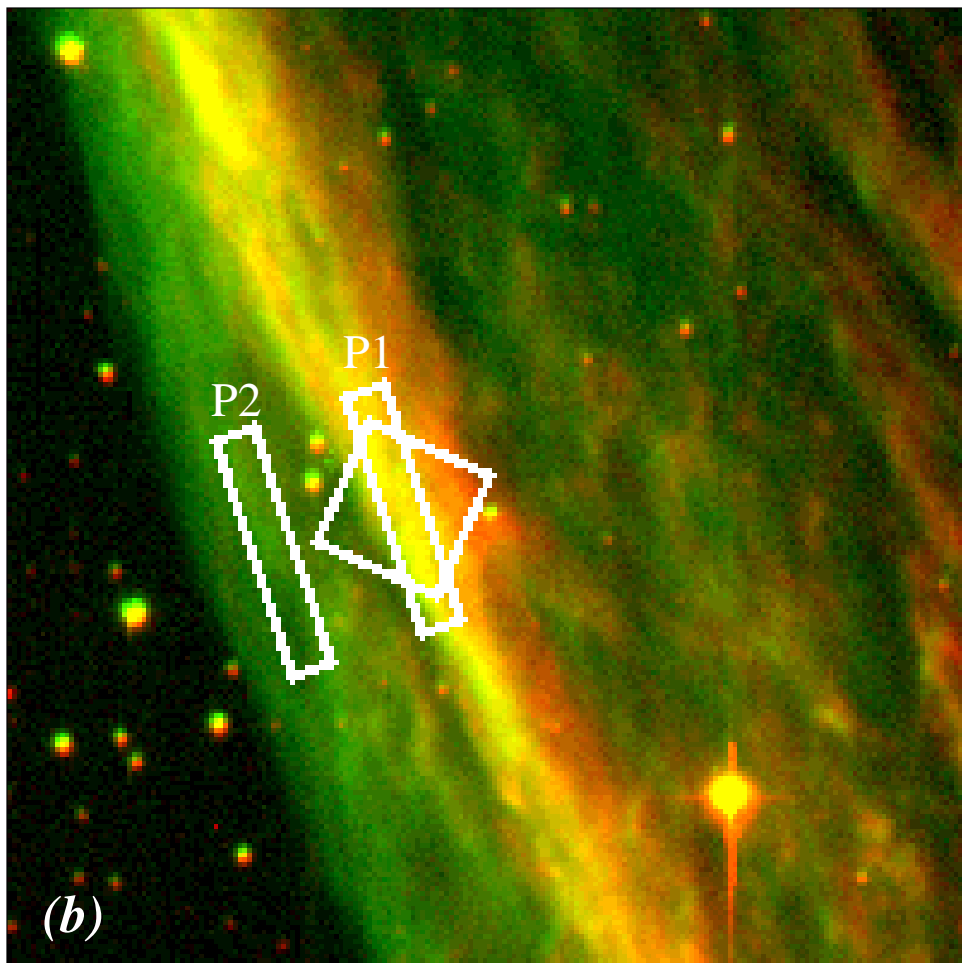
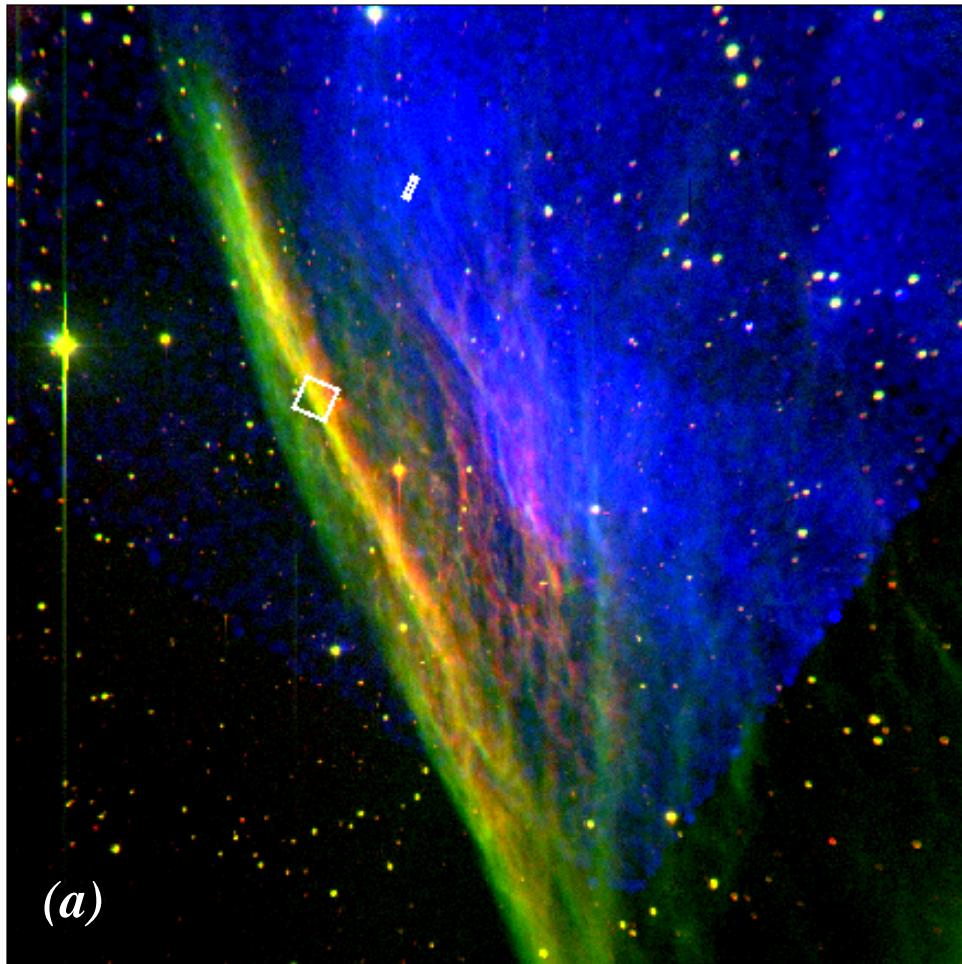
Table 5. UV Spectra Compared with Shock Models

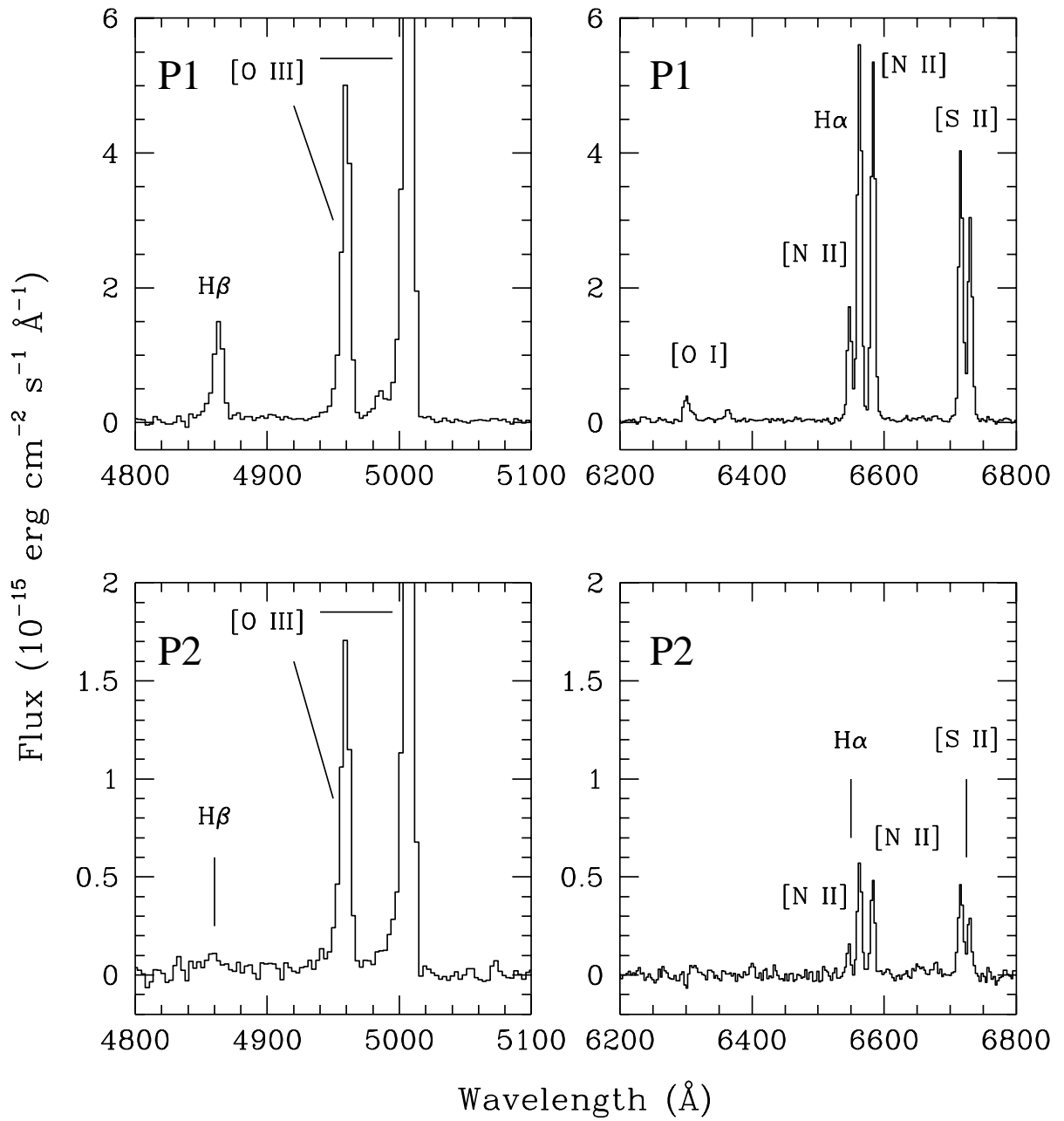
Line ID	$\lambda(\text{\AA})$	I (P1)	M80	M100	M120	M140	M160	M180
S VI	937	12	0	0	2	11	29	30
C III	977	131	1073	1154	1070	528	351	418
N III	991	36	86	88	93	101	67	67
Ne VI]	1006	4	0	0	0	0	2	15
S III	1015	5	5	4	5	4	3	3
O VI	1034	127	0	0	0	12	447	2221
S IV	1070	13	5	7	9	12	7	8
S III	1077	2	2	2	2	2	1	1
Si III	1112	2	14	10	4	3	3	3
Si IV	1125	3	3	4	2	1	1	1
Ne V] ^a	1146	3	0	0	1	4	20	45
C III	1176	6	12	14	13	7	4	5
N V	1240	17	0	1	14	81	229	184
C II	1335	14	263	243	210	96	80	89
O V	1371	<2	0	0	1	4	20	32
Si IV	1396	30	129	113	47	23	22	26
O IV]	1403	44	9	49	85	131	183	191
N IV] ^b	1490	13	6	20	30	46	34	30
C IV	1549	85	83	398	711	638	317	360
He II	1640	37	4	19	44	38	33	36
O III]	1664	100	100	100	100	100	100	100
N III]	1750	41	42	41	42	39	27	27
I(O III)] ^c	1664	...	0.33	0.45	0.61	1.21	1.53	1.56

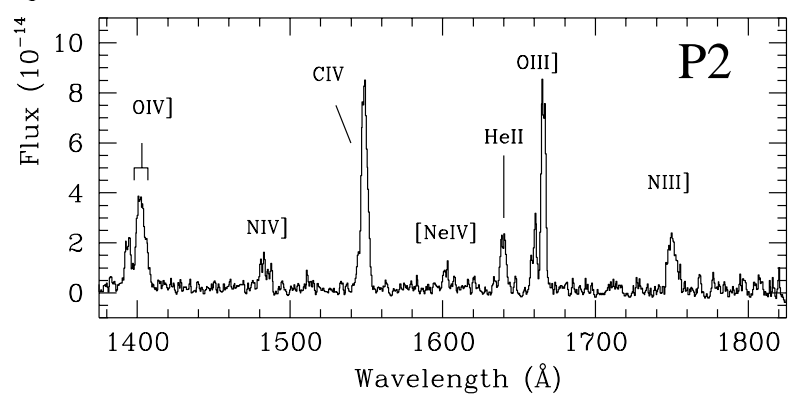
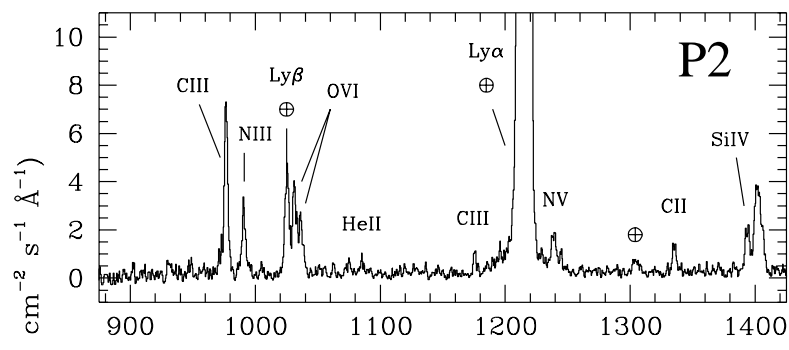
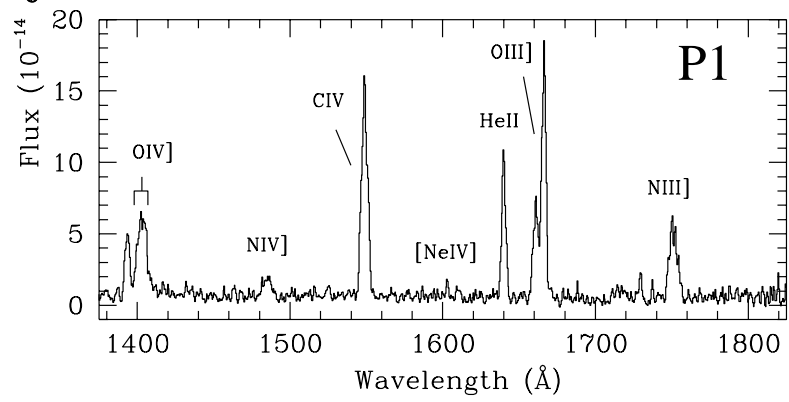
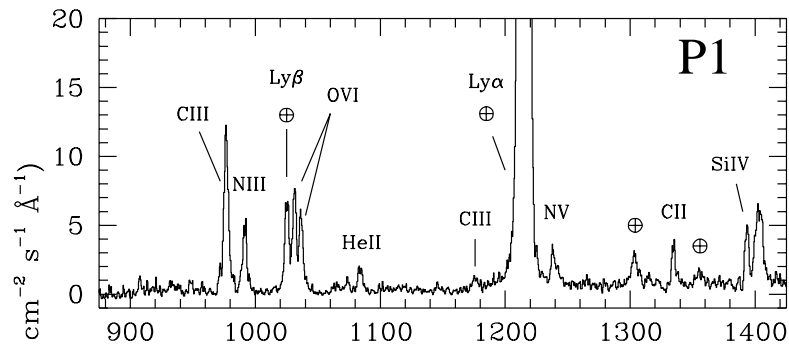
^aSum of 1137Å and 1146Å lines.

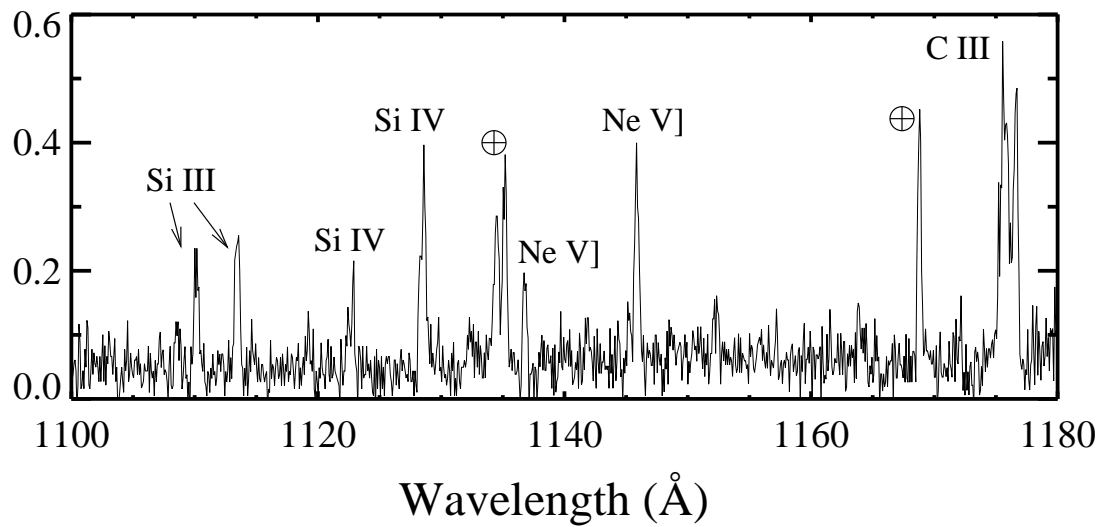
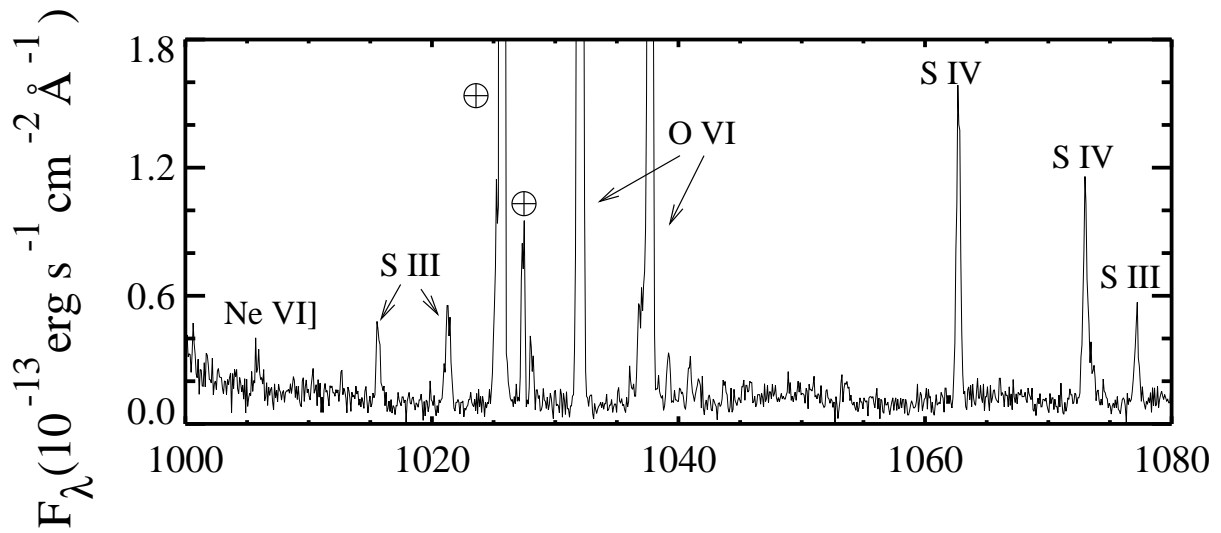
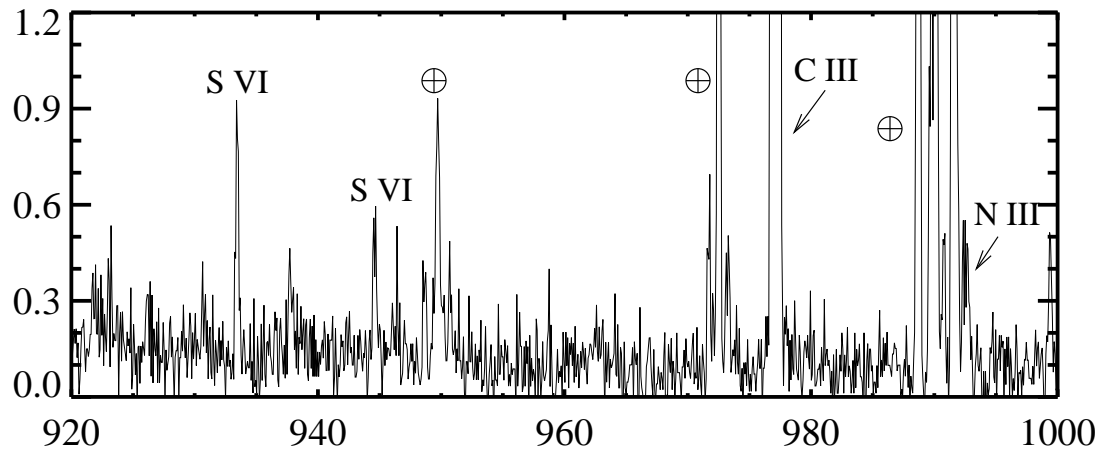
^bIncludes decays from both 3P_1 and 3P_2 states; the latter is a forbidden transition.

^cFlux emerging from the shock front 10^{-5} erg s $^{-1}$ cm $^{-2}$, emitted into 2π steradians.









Wavelength (Å)

